Label-free 3D computational imaging of spermatozoon locomotion, head spin and flagellum beating over a large volume

Authors: Mustafa Ugur Daloglu[1,2,3,§], Wei Luo[1,2,3,§], Faizan Shabbir[1], Francis Lin[2], Kevin Kim[4], Inje Lee[2], Jiaqi Jiang[5], Wenjun Cai[6], Vishwajith Ramesh[2], Mengyuan Yu[7], and Aydogan Ozcan[1,2,3,8,*]

Affiliations:

[1]Electrical Engineering Department, University of California, Los Angeles, CA, 90095, USA.

[2]Bioengineering Department, University of California, Los Angeles, CA, 90095, USA.

[3]California NanoSystems Institute (CNSI), University of California, Los Angeles, CA, 90095, USA.

[4]Chemistry and Biochemistry Department, University of California, Los Angeles, CA, 90095, USA.

[5]Department of Physics and Astronomy, University of California, Los Angeles, CA, 90095, USA.

[6]Department of Mathematics, University of California, Los Angeles, CA, 90095, USA.

[7]Computer Science Department, University of California, Los Angeles, CA, 90095, USA.

[8]Department of Surgery, David Geffen School of Medicine, University of California, Los Angeles, CA, 90095, USA.

§ The authors contributed equally to this manuscript

* Correspondence: Prof. Aydogan Ozcan

E-mail: ozcan@ucla.edu

420 Westwood Plaza, Engr. IV 68-119, UCLA

Los Angeles, CA 90095, USA

Tel.: +1(310)825-0915, Fax: +1(310)206-4685

Supplementary Information

1- Supplementary Figures:

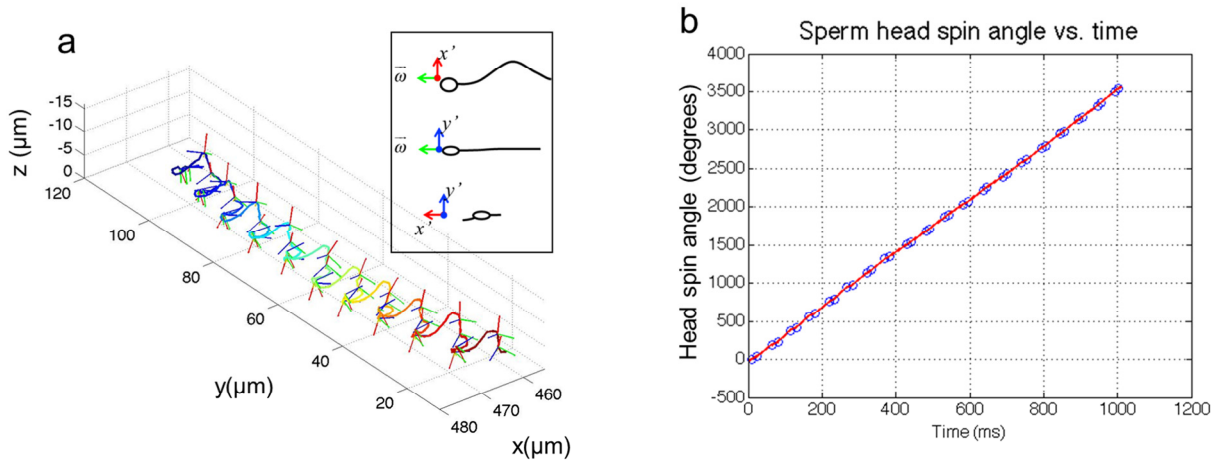

Supplementary Figure S1. (a) Dynamic transformation of the local coordinate system at each phase wrapping event across the trajectory is illustrated. The inset shows the definition of the local coordinate system. **(b)** Head spin angle determination by interpolating subsequent phase wrapping events (one from each perspective) along the time line.

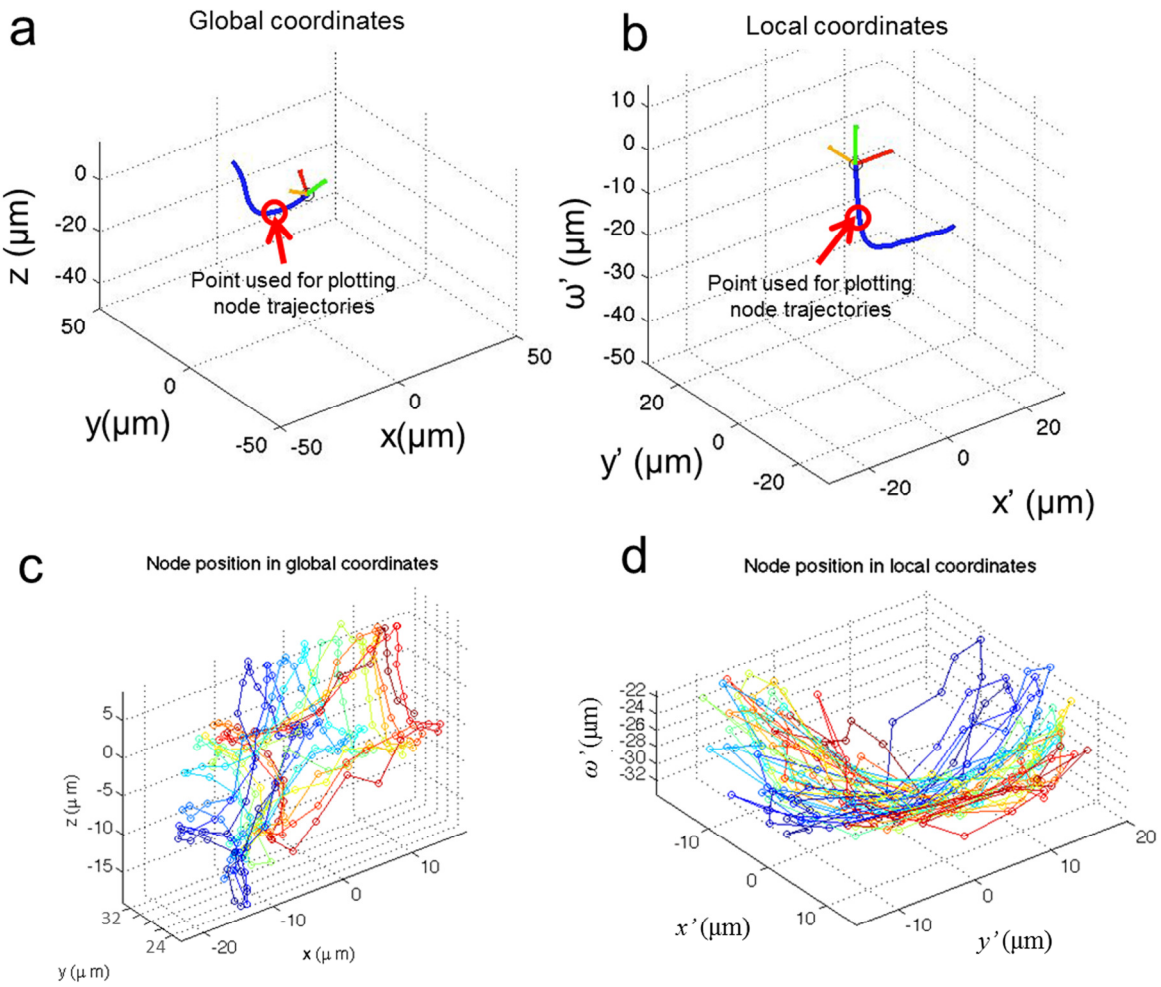

Supplementary Figure S2. Flagellar beating in global and local coordinates. **(a)** and **(b)** Sperm head and flagellum motion for a helix mode sperm in global and local coordinate systems, respectively. The comparison of the flagellar beating in the global and local coordinates is available as Supplementary Movie M6. The translational motion of the sperm is accounted for by placing the head-flagellum junction at the origin for each frame. **(c)** and **(d)** The trail of a flagellum node that is 40 μm (in arc length) away from the head-flagellum junction, tracked in global coordinates and local coordinates, respectively. De-coupled from the head spin, the flagellar beating appears less circular and more confined to the local $\boldsymbol{x'\text{-}\vec{\omega}}$ plane, even for helix mode sperms that are away from the chamber surfaces.

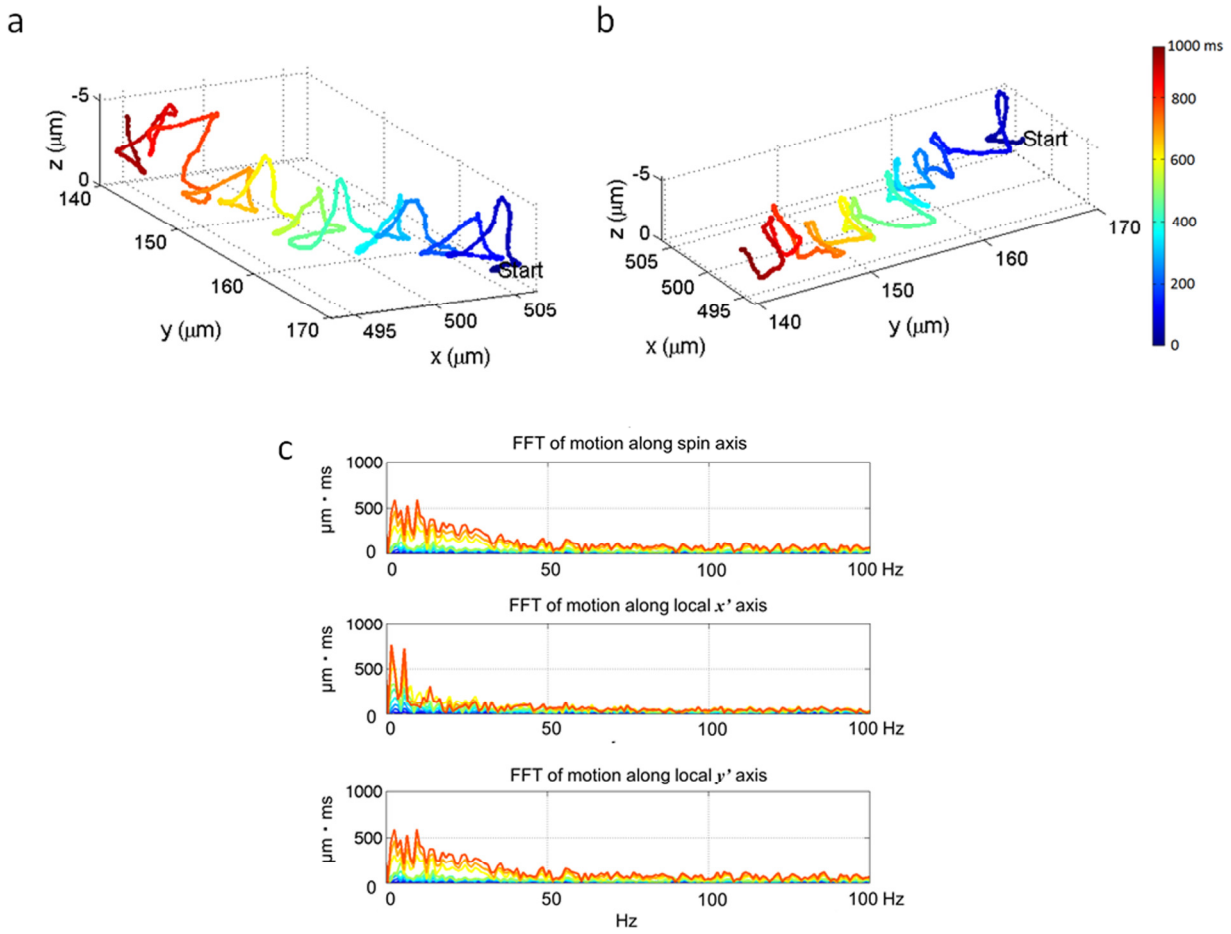

Supplementary Figure S3. The **random type** (Supplementary Movie M3) bovine sperm trajectory and harmonic analysis of its flagellum beating pattern. **(a)** and **(b)** The sperm head trajectory in the global coordinate system. **(c)** Fourier transform of the flagellum node motion along the local coordinate axis with respect to time. Warmer color corresponds to the nodes that have a longer arc length from the head-flagellum junction (see Figure 8a of the main text for the specific color coding). The nodes are spaced with equal intervals of 5 μm and their motion is tracked in the local coordinate system.

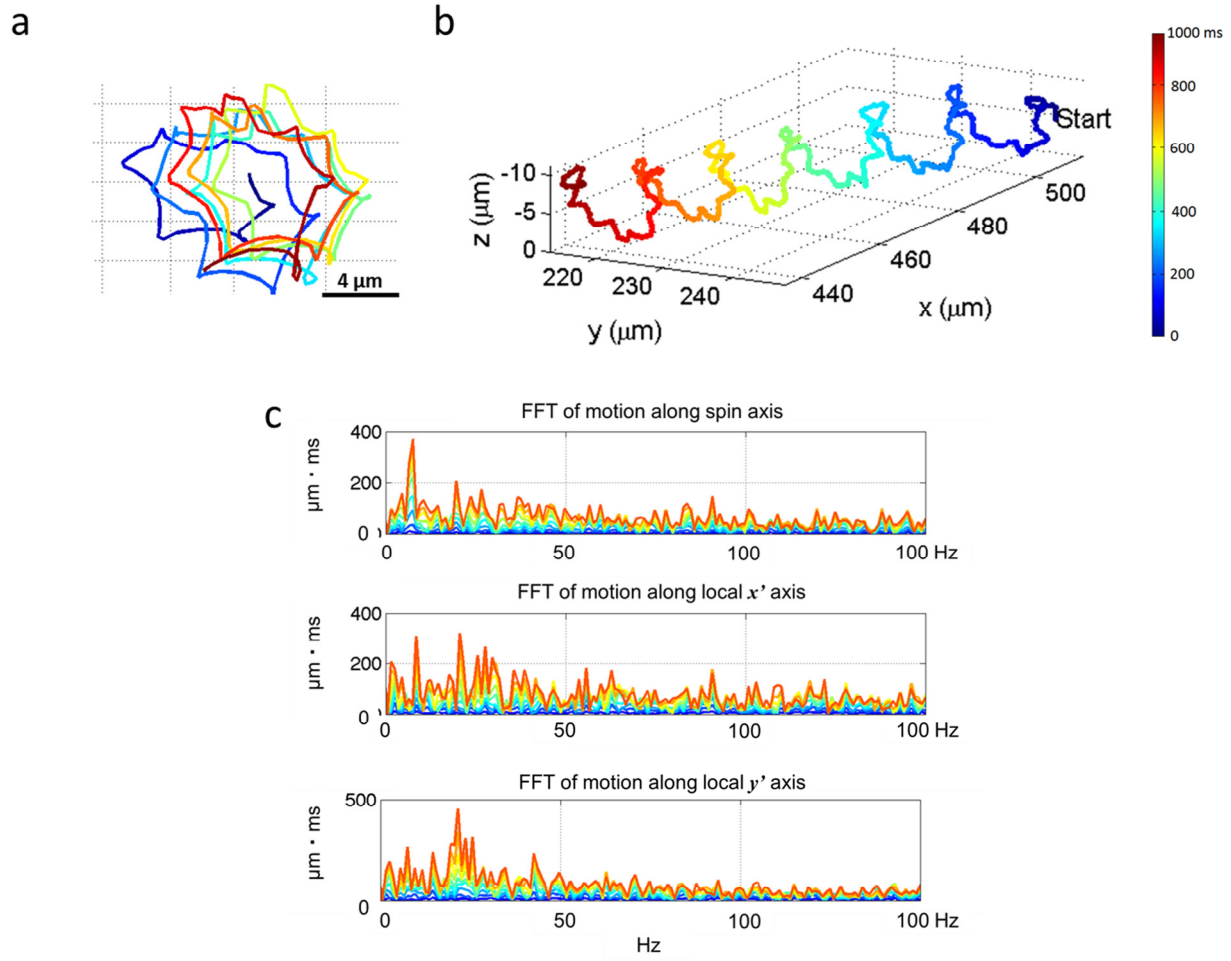

Supplementary Figure S4. Same as Supplementary Figure S3, except for the **helix type** bovine sperm trajectory (also see Supplementary Movie M1).

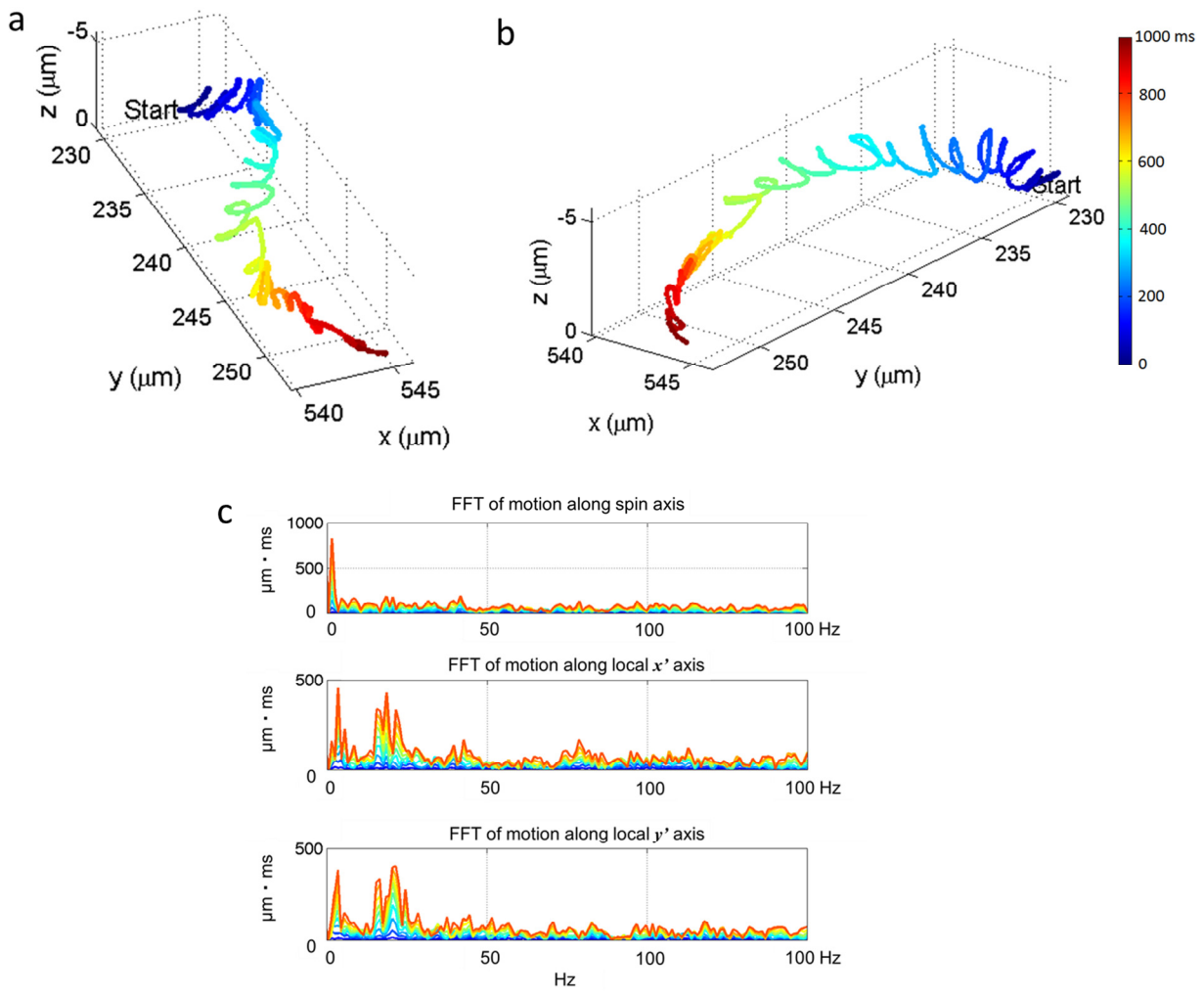

Supplementary Figure S5. Same as Supplementary Figure S3, except for the **twisted ribbon type** bovine sperm trajectory.

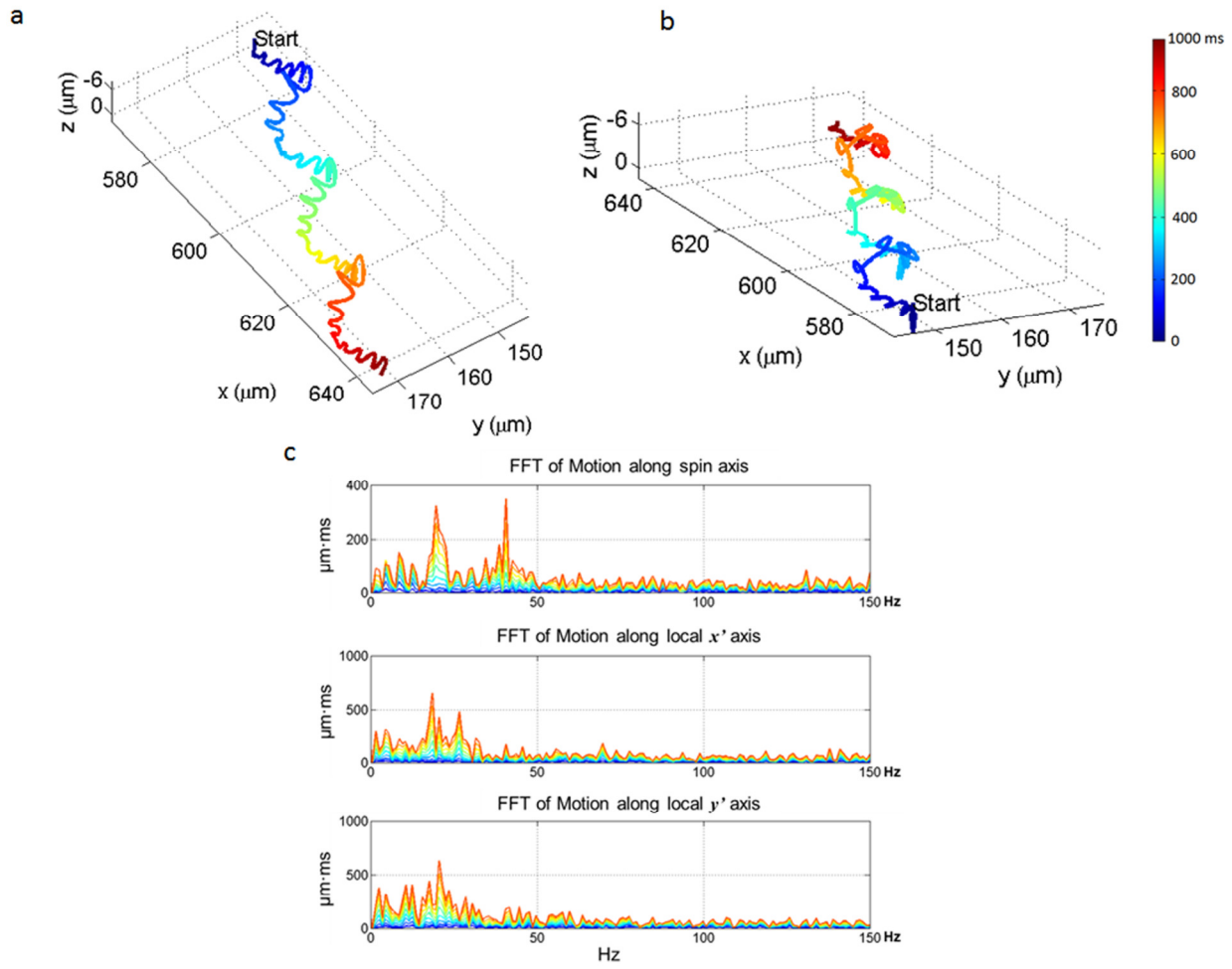

Supplementary Figure S6. Same as Supplementary Figure S3, except for the **helical ribbon type** bovine sperm trajectory (also see Supplementary Movie M4).

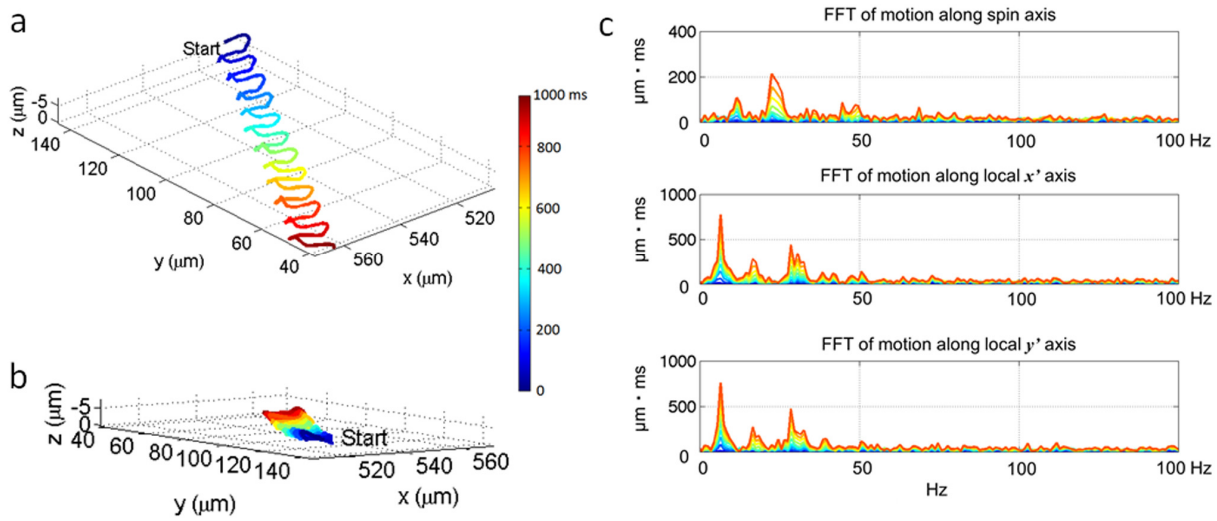

Supplementary Figure S7. Same as Supplementary Figure S3, except for the **flat ribbon type** bovine sperm trajectory (also see Supplementary Movie M5).

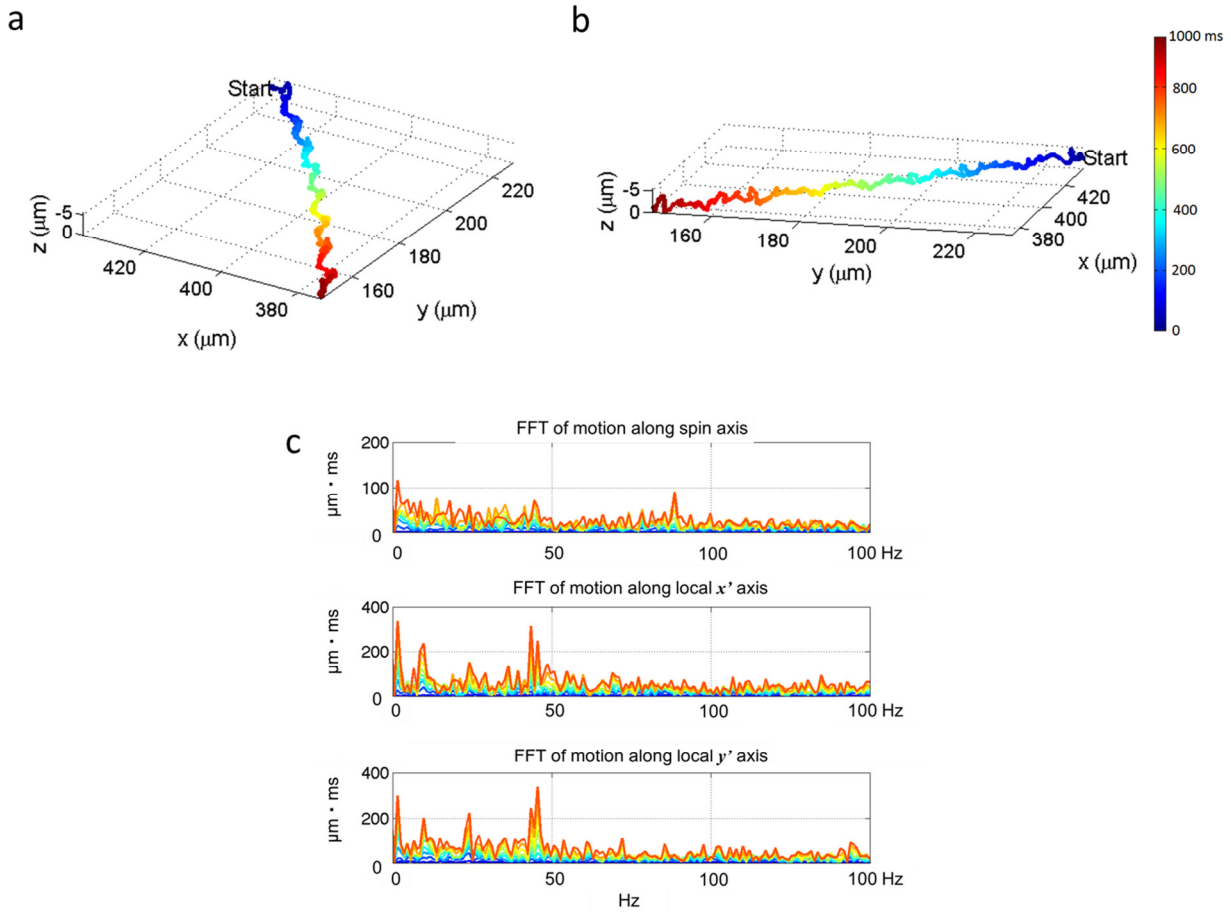

Supplementary Figure S8. Same as Supplementary Figure S3, except for the **straight spin type** bovine sperm trajectory.

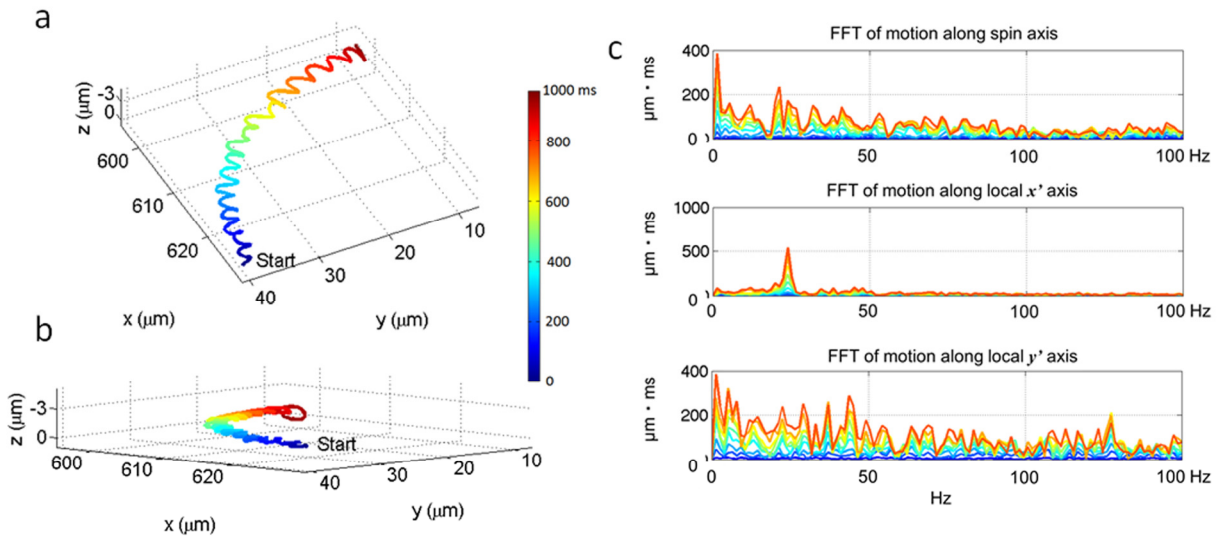

Supplementary Figure S9. Same as Supplementary Figure S3, except for the **slithering type** bovine sperm trajectory (also see Supplementary Movie M2).

2- Supplementary Movies:

Supplementary Movie M1: Helix Type Swimming

https://drive.google.com/open?id=0B5qfXn0m24gyM1VWNV9pZTh3aGs

Supplementary Movie M2: Slithering Type Swimming

https://drive.google.com/open?id=0B5qfXn0m24gyUnI5TlZFeGlJWms

Supplementary Movie M3: Random Type Swimming

https://drive.google.com/open?id=0B5qfXn0m24gyMlkzbzFTRk9SaTg

Supplementary Movie M4: Helical Ribbon Type Swimming

https://drive.google.com/open?id=0B5qfXn0m24gyczFnNU8yY0l1RFk

Supplementary Movie M5: Flat Ribbon Type Swimming

https://drive.google.com/open?id=0B5qfXn0m24gyVEtEbFBPeWpDNGc

Supplementary Movie M6: Flagellar Beating in Global and Local Coordinates

https://drive.google.com/open?id=0B5qfXn0m24gybmJCWkoxamVnMk0

Supplementary Movie M7: Holographic Reconstructions and 2D Flagellar Projections

https://drive.google.com/open?id=0B5qfXn0m24gyWmNQTldlbkFjS2s

3- Calibration of illumination angles in the lens-free optical setup

We calibrate the illumination angles of both oblique sources for each sub-region of interest within our imaging field-of-view. The calibration of the incidence angle is carried out after imaging the sperm samples by introducing an additional vertical illumination besides the two oblique illuminations. The vertical illumination results from a fiber-optic cable with a 100-μm core diameter that is placed approximately 50 cm above the image sensor plane. To ensure the vertical illumination is perpendicular to the image sensor plane, we place a 0.5 mm pinhole mask at the center of the image sensor, and then adjust the optical fiber in horizontal direction so that the reflected light spot from the masked sensor plane overlaps with the fiber's outlet. As a result of these three simultaneous illumination sources, stationary objects at the bottom of the sample chamber generate three holograms during this calibration process. We first back-propagate the vertical hologram with an auto-focusing algorithm to find the optical path length of the object from the image sensor plane. Next, based on a constraint that all the three holographic reconstructions of the object (corresponding to vertical and oblique illumination angles) should overlap after backpropagation through the same layers (i.e., air and bottom cover glass depicted in Fig. 1), we determine the angles of incidence corresponding to both of the oblique illuminations. Taking into account the accuracy of our auto-focusing algorithm (±2.5 μm) and the typical optical path length between the object and image sensor (~400 μm), the accuracy of this angular calibration process is approximately ±0.1°.

4- Definitions of sperm locomotion parameters

The standard definitions of several sperm locomotion parameters used in computer-assisted sperm analysis (CASA) systems are provided below, following Refs. 7 and 10 of main text:

- *Straight-line velocity (VSL)*: The straight-line distance between the starting and ending points of a sperm trajectory, divided by the total duration of motion $(\mu m \cdot sec^{-1})$ [10].
- *Curvilinear velocity (VCL):* The total length of the trajectory covered by the moving sperm divided by the total duration of motion $(\mu m \cdot sec^{-1})$ [10].
- *Linearity*: The ratio between VSL and VCL $(unitless)$ [10].
- *Amplitude of lateral head displacement (ALH)*: Twice the maximum displacement of a sperm head from its moving axis (μm) [10].
- *Beat-cross frequency (BCF)*: The frequency of the sperm head crossing over the middle plane of the "straightened trajectory" (Hz) [10].

5- Analysis of sperm head swimming patterns

The unique 3D capabilities of our platform also enabled us to group bovine sperm head 3D locomotion into 7 major categories (Supplementary Table 1), namely random (32.2%. Supplementary Fig. S3), helix (45%, Supplementary Fig. S4) [1], twisted ribbon (2.4%, Supplementary Fig. S5), helical ribbon (12.1%, Supplementary Fig. S6) [2], flat ribbon (2.1%, Supplementary Fig. S7), straight spin (2.4%, Supplementary Fig. S8), and slithering (3.8%, Supplementary Fig. S9). Note that although more specific swimming patterns could be defined to divide the 'random' category into sub-categories, it is beyond the scope of this manuscript. Some of these locomotion patterns (e.g., twisted ribbon, flat ribbon, and straight spin) were observed quite rarely (<3%) and therefore could only be detected by capturing large numbers of 3D sperm trajectories enabled by our high-throughput imaging platform. Furthermore, flat ribbon and slithering swimming patterns exhibit very similar head translation, and it is the capability to detect the sperm head spin that enabled us to distinguish these two swimming patterns from each other. Among the patterns that showed a rotational trajectory (e.g., helix, twisted and helical ribbon), the majority of the bovine sperm cells exhibited a left-handed rotation (~ 84%) unlike human sperms which prefer right-handed rotation [1]. Note that this rotation reflects the trajectory of the sperm head's center of mass or head-flagellum junction, and should *not* be confused with the angular spin of the head.

	Random	Helix		Twisted ribbon		Helical ribbon		Flat ribbon	Straight spin	Slither
		Left handed	Right handed	Left handed	Right handed	Left handed	Right handed			
Number	687	851	109	36	16	176	82	45	51	80
Percentage	32.2	39.9	5.1	1.7	0.7	8.3	3.8	2.1	2.4	3.8

Supplementary Table. 1 Seven major categories of bovine sperm trajectories. Examples of each trajectory, i.e., random, helix, twisted ribbon, helical ribbon, flat ribbon, straight spin and slithering type, are provided in Supplementary Figs. S3 through S9, respectively.

It is also noteworthy that the VCL and ALH of bovine sperms (Fig. 4) are found to be 3-4 times and ~2 times larger, respectively, compared to those of human sperms [1]. This also

highlights the necessity to have a higher frame-readout rate in recording bovine sperm trajectories without loss of information due to temporal under-sampling. Despite the fast VCL compared to human sperms, it is interesting to note that the VSL of bovine sperms is approximately the same as human sperms. This might be due to the larger asymmetry of the bovine sperm head, which could result in more wobbling as the cell is swimming along its path.

6- Sperm sample preparation

Straws of frozen raw bovine semen (0.25 mL) were purchased (Sexing, TX), and stored between -190°C and -200°C. The motile sperms were separated from the semen following the double layer frozen semen protocol [3], i.e., a density gradient solution was prepared at two different concentrations of 40% (400 µL BoviPure and 600 µL BoviDilute) and 80% (800 µL BoviPure and 200 µL BoviDilute). The gradient was formed by pipetting 500 µL of the 40% solution into a centrifuge tube (Falcon, 25 mL Fisher Scientific) and then pipetting 500 µL of the 80% solution to the bottom. The raw semen extracted from a thawed (30 seconds in 37°C water) straw was gently pipetted on top of the gradient and was centrifuged (Fisher Scientific) for 15 minutes at 300 g. After the centrifugation, the pellet at the bottom of the tube was extracted and gently re-suspended in another centrifuge tube (Falcon, 15 mL Fisher Scientific) containing 1 mL of BoviWash (Nidacon, Sweden) solution. This suspension was centrifuged for 5 minutes at 300 g and the pellet at the bottom of the tube was extracted. The pellet (approximately 10 µL) was re-suspended and diluted in 90 µL of BoviWash resulting in a dilution factor of 10. This solution was further diluted by a factor of 100-200 in BoviWash for imaging experiments. The resulting solution mainly consists of motile sperm cells inside a relatively uniform medium, separated from the seminal plasma and other debris that would otherwise interfere with the holographic image reconstruction process.

7- Lens-free on-chip optical imaging setup

As depicted in Fig. 1, the optical setup of our holographic imaging platform consists of a 13 Mega-pixel, 1.12 μm color CMOS (complementary metal oxide semiconductor) image sensor (IMX135, Sony Corporation, Tokyo, Japan) with a custom-designed high-speed readout circuitry and two oblique illuminations, delivered by two fiber-coupled green LEDs (~525 nm central wavelength with ~20 nm spectral bandwidth). Both of the incidence angles are set to ~18° with mirror symmetry with respect to each other. A chamber filled with sperm samples with a volume of ~34 μL, and sealed with a periodically light blocking mask (see Fig. 1b), is placed on top of the CMOS sensor chip for imaging. Passing through the mask, the simultaneous dual-angle illumination produces two spatially-separated holograms of each individual sperm on top of the image sensor. These holograms are recorded by the image sensor at ~300 frames per second and later used for 3D reconstruction of the entire sperm motion across ~1.8 μL of the sample volume that is placed on the CMOS imager chip (see Fig. 1). This rapid data flow is channeled to a PC (Dell T3600) from the frame grabber through a high-speed PCIe (×4 Gen 2, One Stop Systems) interface, and controlled with a custom-written LabVIEW application. To maintain the sperm samples at a relatively stable temperature of ~35°C during the entire imaging process, the image sensor is turned off for ~10 seconds between successive data acquisition steps.

We would like to emphasize that our lens-free on-chip imaging configuration delivers significantly increased space-bandwidth product (SBP) compared to lens-based systems. For each unit area of an object, the space-bandwidth product of an ideal far-field imaging system is fundamentally limited by the diffraction of light and wave propagation in free space. Optical components (e.g., lenses and opto-electronic sensor-arrays) present “practical” challenges for standard microscope designs to match this diffraction-limited space-bandwidth product, particularly over large sample areas. Computational lens-free on-chip imaging has unique advantages to match the space-bandwidth product dictated by free-space wave propagation since the resolution and sample field-of-view are not directly coupled, unlike its lens-based imaging counterparts.

8- Structured sample chamber

The imaging chambers were constructed using 150 μm thick, plasma cleaned coverslips (Fisher Scientific) with a 500-600 μm silicone spacer (3M Company) in between. The glass slides used as the top cover were pre-deposited with ~4 mm long, ~450 μm wide light blocking stripes (see Fig. 1b and 1c) with a periodicity of ~900 μm. The dual angle illumination passes through the blank regions of the mask and forms evenly distributed bright stripes on top of the image sensor chip. The width of the blank regions and the illumination angles of our set-up are carefully adjusted such that these stripes cover the entire image sensor with minimum spatial overlap. Although implementing these light blocking stripes sacrifices the effective field-of-view of our set-up by a factor of ~2, it comes with two significant benefits: (1) the holograms of the sperm cells from each perspective are now spatially separated, which eliminates the cross-talk between dual angle holographic reconstructions; and (2) the image sensor's full dynamic range and sensitivity are individually reserved for one of the two projections maximizing the SNR and contrast of the sperm holograms and their digital reconstructions. Using these enhanced holograms from two perspectives, we reconstruct the sperm locomotion in 3D following a three-stage procedure, which will be detailed in the following sub-sections, starting with Stage I.

9- Holographic reconstruction of flagellum projections from each perspective – Stage I

First, an average of ~100-200 frames is subtracted from each individual frame to remove the holograms of stationary objects such as immotile sperms or dust particles in the setup. Each frame, with 1.12 μm native pixel pitch, is then interpolated to a grid size of e.g., 0.187 μm to apply a 2D phase modulation, corresponding to the phase front of a plane wave with the correct wavelength (~525 nm) and angle of incidence (~ ±18°) which is carefully calibrated for each ROI within our large FOV. These frames are then digitally back-propagated to the corresponding height of each sperm cell using the angular spectrum approach [4]. After removing the phase-modulation from the back-propagated frames, a pair of 2D projections (including the head and flagellum) with two different perspectives is obtained for all the sperm cells in the imaging volume, i.e., ~1.8 μL of the entire sample volume on sample holder, 34 μL. As detailed in the Results and Discussions section, we also extend the same holographic reconstruction to the neighboring heights (i.e., ±15 μm in depth) to take into account the 3D nature of the flagellum, and avoid out-of-focus imaging related early termination of the 2D skeleton fitting process (see e.g., Supplementary Movie M7 for raw lens-free holograms and the corresponding holographic reconstructions together with the 2D flagellar projections that are reconstructed). As an alternative approach, holographic reconstruction techniques with extended depth-of-focus [5,6] could potentially be used to generate a single, fully focused 2D flagellar reconstruction, constraining the skeleton fitting process to a single height.

10- 3D flagellum reconstruction using a pair of 2D projection images – Stage II

A pair of 2D projections corresponding to two oblique illumination angles is sufficient to determine the 3D structure of the flagellum assuming that the image depth-of-field, contrast and SNR for each perspective are sufficiently large. We adopt the following terminology to better describe this process. First, we name the plane that is defined by the two illumination directions as the "illumination plane". The illumination directions are adjusted such that the illumination plane is perpendicular to the image sensor plane and parallel to the longer edge of the FOV. Second, we define a global Cartesian coordinate system (as depicted in Fig. 5), where the ***x-y*** plane is parallel to the image sensor plane, the ***x*** axis is parallel to illumination plane, and the ***z*** axis is perpendicular to the image sensor plane.

Based on this global coordinate system, notice that for each point O (i.e., an infinitesimal sub-segment on the 3D flagellum, see Fig. 2), there are two separate projections on the ***x-y*** plane, namely P1 and P2, that share the same value on the ***y*** axis. This suggests that the 3D structure of the flagellum can be reconstructed by pairing points which share the same *y* value along the two 2D projections, such as P1 and P2, and triangulating the corresponding 3D origin point, O, with the illumination angles (see Fig. 2). This method works well and provides a unique 3D solution for the functional form of the flagellum when both of the 2D projections can be considered as single-valued functions of *y*. The question of *non-uniqueness* arises when there is more than one pair of points that share the same *y* value. To mitigate such ambiguity, we have developed a point-tracking algorithm that is composed of 4 steps (see Fig 3b), as detailed below.

Step 1: Take two 2D flagellum projections, denoted as $q_1(r_1) = (x_1(r_1), y_1(r_1))$ and $q_2(r_2) = (x_2(r_2), y_2(r_2))$, where r_i (i = 1, 2) is the arc length between the current point $q_i(r_i)$ and the starting point $q_i(0)$ (e.g., *defined by the sperm head-flagellum junction*). We further assume there exists no r_1 and r_2 such that $\frac{dy_1}{dx_1}(r_1) = \frac{dy_2}{dx_2}(r_2) = 0$ *and* $y_1(r_1) = y_2(r_2)$, which represents a relatively unlikely and momentary situation where a section of the sperm flagellum is parallel to the illumination plane. Even if this happens momentarily for a small section of the flagellum, the other points on the flagellum will not be affected, and we can still reconstruct the rest of the 3D flagellum at that time point.

Step 2: Choose one of the projections (e.g., projection 1 in Fig. 3b), as the "tracing path" to guide the point-by-point pairing process along the two projections (1 and 2) with incremental steps along the skeleton of each projection. For the i^{th} node $q_1(r_1^i) = (x_1(r_1^i), y_1(r_1^i))$, on the "tracing path" that is r_1^i away from the origin (in arc length defined by the red paths highlighted in Fig. 3), we search along the second projection to find a point with the corresponding arc length of r_2^i, such that $y_1(r_1^i) = y_2(r_2^i)$, pairing $q_1(r_1^i)$ with $q_2(r_2^i)$. These two matched points are then back projected to the corresponding 3D point: O_i.

Step 3: In case r_2^i cannot be uniquely defined in Step 2, which could happen when two or more points on this flagellum projection have the same *y* value (see Fig. 3), we denote these multiple solutions for node *i* as $r_{2_j}^i$ (*j*=1,2…*J*), where $y_1(r_1^i) = y_2(r_{2_1}^i) = y_2(r_{2_2}^i) = \ldots = y_2(r_{2_J}^i)$. Among these *J* potential solutions, we choose the point $q_2(r_{2_j}^i)$ with the smallest value from $\{r_{2_j}^i \mid j = 1,2, \ldots, J\}$ to pair with $q_1(r_1^i)$. We then continue traversing along projection 1, paring $q_1(r_1^i)$ and $q_2(r_2^i)$ in a similar manner until all the points in each perspective are paired with each other.

Step 4: If the tangential vector at the paring points on projection 2 becomes parallel to the illumination plane, i.e., $\frac{dy_1}{dx_1}(r_1^i) \neq 0 \; and \; \frac{dy_2}{dx_2}(r_{2i}) = 0$ for some node *i,* this indicates that $y_1(r_1^i) = y_2([r_2^i, r_2^{i\prime}])$ for some continuous interval $[r_2^i, r_2^{i\prime}]$. We then switch from the current point $q_1(r_1^i)$ to $q_2(r_2^i)$, in other words switch the two perspectives with each other, and from that point on, traverse through q_2 (i.e. define q_2 as the new "tracing path") and find the matching points on q_1. As a result, the continuous interval $[r_2^i, r_2^{i\prime}]$ can be completely matched with points on $q_1(r_1^i)$ and there is no missing part on the reconstructed 3D sperm flagellum. We repeat Steps 1 through 4 through the entire flagellum to uniquely reconstruct its 3D functional form at a given time point, and at a frame rate of ~300 fps.

11- Detection and quantification of sperm head spin – Stage III

An interesting phenomenon is observed in some of the reconstructed trajectories where the phase signal from the sperm head reconstruction on both of the holographic projections exhibits periodic wrapping events over time (see Fig. 6). Such alternating phase wrapping events on the two projections indicate that the sperm's head is spinning around its own axis while swimming in 3D. To automatically detect and analyze the sperm head spin, we simplify the shape of a bovine sperm head as a tri-axial scalene ellipsoid as shown in Fig. 5, whose longest semi-principal axis (pointing outwards from the paper/screen plane) starts from the head-flagellum junction and connects to the front tip of the sperm head. This longest axis also happens to be the spin axis of the sperm head. When the light penetrates the sperm head through the second-longest semi-principal axis (the "thick" side), the phase change over the corresponding optical path length is larger than π and thus phase wrapping occurs on the 2D holographic reconstruction, while this is not the case for the light travelling through the shortest semi-principal axis (i.e., the thinner side).

The detection of the spin direction and its angular speed can be deduced from the timing of successive phase wrapping events on our holographic projections. To explain how the spin direction is determined, we start with the simplest case, where the spin axis is perpendicular to the illumination plane, thus parallel to the sensor (***x-y***) plane (as defined in the previous sub-section). The time difference between the two phase wrapping events for the two projections is caused by the azimuthal angle difference of the two light sources around the spin axis, and could be mathematically described using a Cartesian coordinate system, where $\overrightarrow{\boldsymbol{\omega}}$ is the unit vector of the spin axis pointing from the head-flagellum junction towards the tip of the head, $\boldsymbol{x'}$ is the unit vector along the "thick" side of the sperm head, $\boldsymbol{y'}$ is the unit vector along the "thin" side of the sperm head and $\widehat{\boldsymbol{k_1}}$, $\widehat{\boldsymbol{k_2}}$ are unit vectors corresponding to the first and second light sources, respectively (see Fig.5). A phase wrapping event occurs on the reconstructed phase image of projection 1 or projection 2 whenever the thick side of the sperm head $\boldsymbol{x'}$ coincides with the "light direction" $\widehat{\boldsymbol{k_1}}$ or $\widehat{\boldsymbol{k_2}}$. Tracking the time difference between these successive phase wrapping events on these two projections, $\Delta t = t_2 - t_1$, and with the known angular difference between the light sources, $\Delta\theta = \theta_2 - \theta_1$, the angular velocity (ω) of the head spin can be calculated as:

$$\omega = \frac{\Delta\theta}{\Delta t} = \frac{\theta_2 - \theta_1}{t_2 - t_1} \quad \text{(Eq. 1)}$$

From the perspective of an observer facing the direction of $\vec{\boldsymbol{\omega}}$, the direction of the head spin is right handed if ω>0 and left handed if ω<0.

Defining a local coordinate system for tracking the head spin and analyzing the flagellar beating patterns

Although we described a methodology to track the sperm head spin and the corresponding local coordinate axis with the angular position information, as discussed above, this was with the assumption that the spin axis remains parallel to the sensor plane throughout the sperm's motion. For freely swimming sperm, however, it is observed that the spin axis also changes with time having components both parallel and vertical to the sensor plane. *We have expanded our method further to incorporate these changes in the spin axis by applying a coordinate transformation between the successive phase wrapping pairs*. To do so, we first define a local coordinate system using the three semi-principal axes of the sperm head ellipsoid. For this, we choose the longest axis of the ellipsoid (i.e., the spin axis of the sperm head) as the local $\vec{\boldsymbol{\omega}}$ axis. Its orientation is determined by connecting the center of the sperm head and head-flagellum junction. We then define the local ***x'*** axis as the longer semi-minor axis of the ellipsoid, and the local ***y'*** axis as the shorter semi-minor axis. When the light traverses through the sperm head in parallel to the local ***x'***-$\vec{\boldsymbol{\omega}}$ plane, it undergoes the largest optical path length, which causes a phase wrapping event in the phase channel of the 2D holographic reconstruction. Therefore, the local coordinate system can be directly defined at the frames which capture phase wrapping events: the local ***x'*** axis lies within the plane defined by the spin axis and the corresponding illumination, and the local coordinates of the intermediate frames can be determined by interpolating the spin angles between two phase wrapping events. And to measure the spin angle between two successive phase wrapping events, we first determine the two corresponding local coordinate systems, namely $\{x'_1, y'_1, \vec{\boldsymbol{\omega}}_1\}$ and $\{x'_2, y'_2, \vec{\boldsymbol{\omega}}_2\}$, and then overlap the two spin axes (i.e., $\vec{\boldsymbol{\omega}}_1$ and $\vec{\boldsymbol{\omega}}_2$) of these two coordinates by rotating $\vec{\boldsymbol{\omega}}_1$ within the $\vec{\boldsymbol{\omega}}_1 - \vec{\boldsymbol{\omega}}_2$ plane. This rotation will transform $\{x'_2, y'_2, \vec{\boldsymbol{\omega}}_2\}$ into $\{x'_{2,rot}, y'_{2,rot}, \vec{\boldsymbol{\omega}}_1\}$, where the angle formed by $x'_{2,rot}$ and x'_2 (or $y'_{2,rot}$ and y'_2) is considered as the transformation angle.

This transformation of the local coordinate systems throughout the 3D locomotion of the sperm is very important for better understanding flagellar motion and its 3D beating patterns as it decouples the head locomotion and its spin from flagellar beating patterns (refer to the Results and Discussions section for further discussion on this). Based on this local coordinate transformation, we can simply express the coordinates of any point along the sperm flagellum according to the local coordinate system with a different transformation matrix at each time frame. This capability enabled us to visualize the flagellar motion in an isolated and unique way, i.e., from the perspective of an observer located at and traveling with the sperm head – see e.g., Figs 8 and 9, Supplementary Movies M1 through M6, which are discussed in detail in our Results and Discussions section.

12- Reconstruction platform

The numerical reconstructions from raw holographic images recorded by the image sensor chip were performed using MATLAB with Parallel Computing Toolbox (Version 2012a, MathWorks, MI, USA) on two machines, each equipped with four eight-core 2.13-GHz central processing unit, CPU (Intel Xeon E7-4830) and 1 TB random access memory. The total computation time can be broken into two main parts. The first one is the holographic reconstruction of flagellum projections on both perspectives, where the reconstruction process (including the phase retrieval) using a single CPU core costs approximately 12.1 seconds for each frame. The second one is the 2D flagellum projection fitting and 3D flagellum reconstruction process: a single sperm at each frame costs approximately 5.1 seconds using one CPU core. Therefore, for a typical 300-frame motion of a single sperm, the reconstruction using a single CPU core costs approximately 86 minutes. Using the parallel computing configuration, the overall computation time for all the 2133 sperms using the aforementioned computing platform takes approximately 48 hours. Considering that our holographic reconstruction heavily relies on 2D fast Fourier transforms, and that the reconstructions of all the frames are independent from each other, implementing our 3D reconstruction algorithm on graphics processing units (GPUs) could bring significant parallelization and improvement in computation time, by e.g., 10 to 20-fold [7]. Furthermore, a significant additional reduction in the total reconstruction time can be achieved by using other programming languages such as C or C++ instead of MATLAB.

13- References

1. Su, T.-W., Xue, L. & Ozcan, A. High-throughput lensfree 3D tracking of human sperms reveals rare statistics of helical trajectories. *Proc. Natl. Acad. Sci.* **109,** 16018–16022 (2012).
2. Su, T.-W. *et al.* Sperm Trajectories Form Chiral Ribbons. *Sci. Rep.* **3,** (2013).
3. Samardzija, M. *et al.* A comparison of BoviPure® and Percoll® on bull sperm separation protocols for IVF. *Anim. Reprod. Sci.* **91,** 237–247 (2006).
4. Goodman, J. W. *Introduction to Fourier optics*. (Roberts & Co, 2005).
5. Colomb, T. *et al.* Extended depth-of-focus by digital holographic microscopy. *Opt. Lett.* **35,** 1840–1842 (2010).
6. Matrecano, M., Paturzo, M. & Ferraro, P. Extended focus imaging in digital holographic microscopy: a review. *Opt. Eng.* **53,** 112317 (2014).
7. Isikman, S. O. *et al.* Lens-free optical tomographic microscope with a large imaging volume on a chip. *Proc. Natl. Acad. Sci.* **108,** 7296–7301 (2011).